Title

TANGLED1 mediates microtubule interactions that may promote division plane positioning in maize

Running title

TANGLED1 microtubule interactions during division

Authors

Pablo Martinez[1], Ram Dixit[2], Rachappa S. Balkunde[2], Antonia Zhang[3], Seán E. O'Leary[1,3], Kenneth A. Brakke[4], Carolyn G. Rasmussen[1,5,6]

ORCID

PM 0000-0003-4846-4958
RD 0000-0001-7881-2859
RSB 0000-0002-6059-9532
AZ 0000-0001-9819-1447
SEO'L 0000-0002-1214-949X
KAB 0000-0001-6983-4503
CGR 0000-0002-4354-6295

[1]Biochemistry and Molecular Biology Graduate Program, University of California, Riverside, California 92521, USA

[2]Department of Biology and Center for Engineering Mechanobiology, Washington University in St. Louis, St. Louis, MO 63130, USA

[3]Department of Biochemistry, University of California, Riverside, California 92521, USA

[4]Department of Mathematics, Susquehanna University, Selinsgrove, Pennsylvania 17870, USA

[5]Department of Botany and Plant Sciences, Center for Plant Cell Biology, Institute for Integrative Genome Biology, University of California, Riverside, CA 92521, USA

[6]Correspondence to carolyn.rasmussen@ucr.edu

Keywords

maize, microtubule, phragmoplast, mitosis, PPB, spindle, TANGLED1

Summary

TAN1 is a microtubule-binding protein required for the spatial control of plant division plane orientation. TAN1 mediates both lateral and end-on microtubule interactions in vitro. These activities may promote proper division plane orientation in vivo.

Abstract

The microtubule cytoskeleton serves as a dynamic structural framework for mitosis in eukaryotic cells. TANGLED1 (TAN1) is a microtubule-binding protein that localizes to the division site and mitotic microtubules and plays a critical role in division plane orientation in plants. Here, in vitro experiments demonstrate that TAN1 directly binds microtubules, mediating microtubule zippering or end-on microtubule interactions, depending on their contact angle. Maize *tan1* mutant cells improperly position the preprophase band (PPB), which predicts the future division site. However, cell-shape-based modeling indicates that PPB positioning defects are likely a consequence of abnormal cell shapes and not due to TAN1 absence.. In telophase, co-localization of growing microtubules ends from the phragmoplast with TAN1 at the division site suggests that TAN1 interacts with microtubule tips end-on. Together, our results suggest that TAN1 contributes to microtubule organization to ensure proper division plane orientation.

Introduction

The proper organization of microtubule networks during interphase and mitosis is important to promote growth and development at both the cell and organismal levels (Wasteneys and Ambrose, 2009; Elliott and Shaw, 2018; Ehrhardt and Shaw, 2006; Baskin et al., 2004). Mechanisms for achieving and modulating microtubule organization are driven by microtubule-microtubule or microtubule-protein interactions: zippering at low contact angles (Ho et al., 2012; Tulin et al., 2012; Smertenko et al., 2004; Shaw et al., 2003), contact-mediated catastrophe (Dixit and Cyr, 2004), severing (Lindeboom et al., 2013; Zhang et al., 2013; Panteris et al., 2018; Komis et al., 2017) and stabilization at cell edges (Ambrose et

al., 2011). These processes alter microtubule dynamics and organization. Mitotic microtubule structures are formed and modified by these activities to perform a distinct role in DNA segregation and separation of daughter cells. In plants, the key mitotic structures are the preprophase band (PPB), metaphase spindle, and phragmoplast. Proteins which regulate the formation and function of these structures are localized along these different structures as well as the cortical plant division site.

During the G2 phase of the cell cycle, the preprophase band (PPB) is formed as a ring-shaped arrangement of microtubules, actin and associated proteins that localize just under the plasma membrane to form the cortical division zone (Smertenko et al., 2017; Van Damme et al., 2007). The PPB is an early marker of the future division site in land plants: it indicates the location where the developing new cell wall will fuse with the mother cell (Rasmussen and Bellinger, 2018; Facette et al., 2019; Pickett-Heaps and Northcote, 1966). Several microtubule associated proteins play an important role in division plane orientation by promoting PPB formation. A large family of proteins with microtubule binding motifs recruit a protein phosphatase type 2A (PP2A) complex to form the PPB (Spinner et al., 2013; Wright et al., 2009; Traas et al., 1995; Spinner et al., 2010; Drevensek et al., 2012; Schaefer et al., 2017). The proper formation and positioning of the PPB may orient the metaphase spindle to promote rapid mitotic progression (Chan et al., 2005; Ambrose and Cyr, 2008; Schaefer et al., 2017). As cells enter metaphase, the PPB is completely disassembled; however a handful of proteins that colocalize with the PPB continue to label the division site until the end of cytokinesis (Walker et al., 2007; Xu et al., 2008; Lipka et al., 2014; Martinez et al., 2017; Li et al., 2017; Buschmann et al., 2015).

During telophase, the phragmoplast is assembled from microtubules, actin, and associated proteins to aid in the formation of the cell plate via vesicle delivery (Smertenko et al., 2017; Smertenko, 2018; Lee and Liu, 2013; Jürgens, 2005b). The phragmoplast expands outwards to the cell cortex through the polymerization of new microtubules from existing leading edge microtubules and depolymerization at the lagging edge as the cell plate is assembled (Murata et al., 2013). The direction of phragmoplast expansion

is thought to be guided by proteins that continuously label the division site (Rasmussen and Bellinger, 2018; Livanos and Müller, 2019). Once the phragmoplast reaches the cortex it is disassembled and the cell plate fuses with the plasma membrane, completing cytokinesis (Jürgens, 2005a; Worden et al., 2012). Mutants with defects in maintaining division plane orientation place new cell walls outside the location originally specified by the PPB. In maize, *tangled1* (*tan1)* mutants have division plane defects in both symmetric and asymmetric divisions (Smith et al., 1996) caused by a failure of the phragmoplast to return to the division site originally indicated by the PPB (Martinez et al., 2017). TAN1-YFP localizes to the cortical division site throughout mitosis in *Arabidopsis* and maize (Martinez et al., 2017; Walker et al., 2007). TAN1 also co-localizes with mitotic microtubule arrays in vivo when fused to YFP (Martinez et al., 2017) and using a non-specific TAN1 antibody (Smith et al., 2001). TAN1 is a highly basic protein without any obvious known domains (Smith et al., 2001). Structure-function analysis identified two highly conserved regions of TAN1 that separately promoted its localization to the division site either during late G2 or telophase (Rasmussen et al., 2011). The protein region promoting TAN1 localization during telophase was subsequently shown to be critical for its function in vivo (Mir et al., 2018).

Double mutants for two kinesin 12 paralogs in *Arabidopsis thaliana*, *phragmoplast orienting kinesin 1 (pok1)* and *pok2* display a severe division plane defect (Müller et al., 2006b). POK1 interacts directly with TAN1 and localizes to the division site (Walker et al., 2007; Lipka et al., 2014; Rasmussen et al., 2011). Both POK1 and POK2 are required for TAN1 localization to the division site after metaphase (Walker et al., 2007; Lipka et al., 2014). POK2 acts as a weak microtubule plus-end-directed motor in vitro (Chugh et al., 2018). Interestingly, in addition to its division site localization, POK2 also accumulates in the phragmoplast midline where it may interact with MICROTUBULE ASSOCIATED PROTEIN65-3, MAP65-3, or other MAP65 proteins (Herrmann et al., 2018; Ho et al., 2011). Another closely related MAP65, MAP65-4, is localized to the PPB, spindle and phragmoplast and the division site (Li et al., 2017). The *map65-3 map65-4* double mutant in *Arabidopsis thaliana* ~~displays a severe~~ has a cytokinesis defect but it is not yet clear whether it has a division plane defect (Li et al., 2017). MAP65-4 regulates

118 microtubule stability by increasing microtubule elongation phases during bundling (Fache et al., 2010)
119 while another related MAP65, MAP65-1, increases microtubule stability by protecting against severing
120 and promoting microtubule flexibility during bundling (Portran et al., 2013; Stoppin-Mellet et al., 2013;
121 Burkart and Dixit, 2019). Microtubule binding and bundling proteins therefore may contribute to the
122 assembly of the mitotic microtubule structures, but also serve as important effectors for the establishment,
123 timely progression and execution of properly oriented plant cell divisions.
124
125 In addition to division plane defects, the *tan1* mutant has mitotic progression delays and reduced plant
126 stature (Martinez et al., 2017; Smith et al., 1996). Mitotic progression delays and phragmoplast guidance
127 defects were mostly uncoupled using a partially rescued *tan1* mutant expressing TAN1-YFP fused to the
128 CYCLIN B-destruction box motif (Martinez et al., 2017). In this partially rescued line, mitotic delays are
129 observed but division plane defects are rare, coinciding with TAN1-YFP signal at the division site, but
130 lack of detectable TAN1-YFP signal in the spindle and phragmoplast. We hypothesize that TAN1 is a
131 multifunctional protein that aids in timely mitotic progression when it localizes to mitotic microtubule
132 structures and maintains division plane orientation via phragmoplast guidance when it is localized to the
133 division site. Here we report an in vitro function for TAN1 in mediating microtubule interactions, and an
134 in vivo function in spindle organization and phragmoplast microtubule interactions at the division site.
135
136 **Results and Discussion**
137 **TAN1 binds to microtubules in vitro**
138 TAN1 protein has been shown to bind to taxol-stabilized microtubules in a blot overlay assay (Smith et
139 al., 2001). To quantitatively assess the binding of TAN1 to microtubules, we recombinantly expressed
140 6xHIS-tagged ZmTAN1 (HIS-TAN1) protein, and tested its ability to bind to microtubules. HIS-TAN1
141 protein bound to taxol-stabilized microtubules in cosedimentation experiments (Figure 1A). Titration of
142 microtubules against a fixed concentration of HIS-TAN1 resulted in saturable TAN1-microtubule
143 binding. Fitting the binding data hyperbolically as in similar studies (Tulin et al., 2012; Wong and

Hashimoto, 2017) yielded a $K_{0.5}$ value of 1.08 μM (95% CIs: 0.722 to 1.43 μM) and suggested that at least 70% of the HIS-TAN1 was active in binding microtubules. This calculated affinity is similar to that of other microtubule-binding proteins (Tulin et al., 2012; Portran et al., 2013; Wong and Hashimoto, 2017). Significantly less than 100% TAN1 saturation was observed at the maximal available microtubule concentration. This could be explained in terms of an inactive protein fraction, but alternatively by a model such as multi-site binding with negative cooperativity (Supplementary Table 1). To directly visualize the binding of TAN1 to microtubules in vitro, we purified recombinant HIS-TAN1-GFP. Unfortunately, this fusion protein was not fluorescent, ~~probably~~ potentially because GFP did not fold correctly during renaturation of recombinant protein from bacterial inclusion bodies. Since HIS-TAN1-GFP still bound to microtubules with similar affinity as HIS-TAN1 (Supplemental Figure 1A), we labeled it with the organic fluorophore Atto488 to visualize it using fluorescence microscopy. When co-incubated with taxol-stabilized rhodamine-labeled microtubules, Atto488-tagged HIS-TAN1-GFP (100 nM) localized along the microtubule lattice (Figure 1D-E). Kymographs of Atto488-tagged HIS-TAN1-GFP showed that it did not move on GMPCPP rhodamine labeled microtubules over ~2 minutes of imaging (Figure 1F-G). Atto488-tagged HIS-TAN1-GFP unfortunately aggregated over the course of microtubule co-sedimentation assays (Supplemental Figure 1B), and therefore we did not use it in further experiments.

Previous results showed that TAN1-YFP co-localizes with microtubules in the PPB, the spindle, and the phragmoplast (Martinez et al., 2017). However, direct TAN1-microtubule binding data suggested that TAN1 will interact with microtubules regardless of cell-cycle stage. To examine TAN1-microtubule interaction in interphase, we transiently expressed both TAN1-GFP and RFP-TUBULIN in non-dividing *Nicotiana benthamiana* epidermal cells using the constitutive *35S* promoter. After three days of incubation, we imaged TAN1-GFP and RFP-TUBULIN using confocal microscopy. TAN1-GFP co-localized with RFP-TUBULIN (Supplementary Figure 2A and 2B), indicating that mitosis-specific proteins are not necessary for TAN1 interaction with microtubules, consistent with our in vitro co-sedimentation assays. No obvious differences in microtubule arrays in interphase epidermal cells were

observed between those infiltrated with RFP-TUBULIN and TAN1-GFP (Supplementary Figure 2A and B) or RFP-TUBULIN only (Supplementary Figure 2C). This lack of obvious changes in microtubule organization contrasts with overexpression of other MAPs such as MAP65-1 (Ho et al. 2012) and CLASP (Kirik et al. 2007). However, TAN1-GFP fluorescent signal was also low, consistent with the hypothesis that TAN1 levels may be post-translationally regulated by degradation (Rasmussen et al., 2011).

TAN1 does not markedly alter microtubule dynamics in vitro

To determine whether TAN1 regulates microtubule polymerization dynamics, we conducted in vitro microtubule polymerization experiments. Microtubules were nucleated from GMPCPP-stabilized microtubule seeds and their polymerization and depolymerization was promoted by adding 17.5 μM tubulin. Microtubule dynamics were visualized using rhodamine-labeled tubulin and total internal reflection fluorescence microscopy (materials and methods). At-lower concentrations of HIS-TAN1 (< 1μM), no significant effect on microtubule dynamics was observed (Table 1). At a concentration of 2 μM HIS-TAN1, which is close to the apparent $K_{0.5}$ of TAN1 for taxol-stabilized microtubules, we observed small decreases in both microtubule plus-end growth and plus-end shrinkage rates (compared to 0μM HIS-TAN1, using the Mann Whitney test, Table 1). HIS-TAN1 addition did not alter the amount of time microtubules spent growing or the frequency of catastrophes. However, small but significant differences in time spent shrinking were observed (compared to 0 μM HIS-TAN1, Table 1). Under the experimental conditions used, rescue events were rare and the minus-ends were not dynamic; therefore, these parameters were not quantified. Together, these results suggest that regulation of microtubule polymerization dynamics is unlikely to be the primary function of TAN1.

HIS-TAN1 mediates lateral and end-on microtubule interactions in vitro

During the course of our in vitro microtubule dynamics experiments, we observed that at high concentrations of HIS-TAN1 (2 μM), microtubules that contacted each other transiently interacted. To promote microtubule interactions, we conducted experiments with a higher concentration of GMPCPP-

196 stabilized seeds and free tubulin dimers (22.5 μM concentration) to generate more microtubules that grew
197 longer and hence encountered each other more frequently. We used 2 μM HIS-TAN1 because it resulted
198 in microtubule interactions (139 interaction events resulting from 506 crossovers) in dynamic microtubule
199 assays, whereas no interactions were observed at lower concentrations of HIS-TAN1 (Table 1). We
200 observed two kinds of microtubule bundling interactions depending on the microtubule contact angle. At
201 small or shallow contact angles (angle = 19.6° ± 7.6°, average ± SD), the microtubules progressively
202 zippered together to produce bundles (n = 47 bundling events out of a total of 139 interactions observed,
203 34% of bundling events) (Figure 2A-2B). Zippering of microtubules in parallel and antiparallel
204 configurations occurred with similar frequencies (n = 13/27 and 14/27 where orientation was
205 unambiguous, respectively). Therefore, TAN1 does not preferentially bundle microtubules in specific
206 orientations. In contrast, MAP65 microtubule bundling proteins preferentially bundle antiparallel
207 microtubules (Gaillard et al., 2008; Tulin et al., 2012). At high contact angles (angle = 60° ± 20°, average
208 ± SD), transient "end-on" microtubule interactions were observed during microtubule depolymerization
209 (Figure 2C-2D, Supplemental Video 1). As one microtubule depolymerized past a previous crossover site,
210 TAN1 mediated an interaction at the crossover point. The depolymerizing end stayed bound to the
211 sidewall of the second microtubule, resulting in a pulling force on the stable microtubule (n = 92 end-on
212 interactions out of a total of 139 interactions observed, 66% of interaction events). Interestingly, highly
213 basic peptides linked together to form an artificial polypeptide capable of multivalent electrostatic
214 interactions with microtubules displayed similar microtubule pulling and bundling activities as TAN1
215 (Drechsler et al., 2019). The intrinsically disordered microtubule-associated protein tau also results in
216 similar microtubule interactions which are thought to depend on tau's multivalent microtubule binding
217 (Kellogg et al., 2018). Based on the similarities in the types of microtubule interactions mediated by the
218 artificial polypeptide, tau and TAN1 and their shared biochemical characteristics of net positive charge
219 and intrinsically disordered regions, we hypothesize that TAN1 likely contains multiple microtubule-
220 binding sites that enable interaction between microtubules. This property would also allow TAN1 to
221 bundle microtubules without requiring dimerization or multimerization in contrast to the bundling protein

MAP65-1 (Ho et al., 2011). Based on these data, we conclude that the outcomes of TAN1-microtubule interactions depend on the initial contact or crossover angle between the microtubules, and that at high contact angles, TAN1-microtubule interactions lead to transient pulling or catching.

Microtubule zippering is a well-characterized form of microtubule bundling in plants, animals and fungi (Dixit and Cyr, 2004; Tulin et al., 2012; Janson et al., 2007; Subramanian et al., 2010; Gaillard et al., 2008). Microtubule end-on interactions have been studied extensively in animals and fungi and typically involve forces generated by motor proteins (Laan et al., 2012b; a). For example, end-on microtubule capture by motor proteins is important for spindle positioning in animals (Kiyomitsu, 2019) and yeast (Gupta et al., 2006). Non-motor dependent mechanisms, such as harnessing the energy of a depolymerizing microtubule, also generate pulling forces (Dogterom et al., 2005; Grishchuk et al., 2005). TAN1, because it lacks canonical motor domains, is unlikely to be a motor protein. However, similar to the microtubule binding protein tau, it is both highly basic and is predicted to contain intrinsically disordered regions when analyzed by the prediction software DisEMBL (Linding et al., 2003).

We were surprised that significant numbers of microtubule interactions were detectable in vitro only with relatively high concentrations of TAN1 (2 μM), when TAN1-MT interactions were detected using GMPCPP-stabilized microtubule seeds at low TAN1 concentrations (100 nM). One potential reason for this apparent discrepancy in binding or interaction could be due to TAN1 binding tubulin dimers in addition to microtubules. Tubulin dimer binding in addition to microtubule binding occurs with proteins such as tau (Fauquant et al. 2011) or Clasp (Al-Bassam et al., 2010). Therefore, we tested whether TAN1 binds soluble tubulin using in vitro affinity chromatography. Tubulin was incubated with HIS-TAN1-GFP and anti-GFP agarose beads. HIS-TAN1-GFP pulled down tubulin while HIS-GFP did not, indicating that TAN1 interacts with tubulin in addition to microtubule polymers (Supplemental Figure 3A). By densitometry analysis, we estimate that one HIS-TAN1-GFP molecule binds to ~two tubulin dimers (n = 3 replicates), indicating that TAN1 contains at least two distinct tubulin-binding regions. We used size

exclusion chromatography to assess whether tubulin was dimeric in the affinity chromatography buffer (BRB80) and temperature conditions (~4 °C). Tubulin eluted with an apparent size of ~110 kDa consistent with tubulin dimerization using both the same concentration of tubulin used for affinity chromatography (5 μM, 91.45 kDa ±12.32 average ± SD) and twice as much (10 μM, 111.13 kDa ± 14.18 average ± SD) (Supplemental Figure 3B and 3C). Overall, this suggests that TAN1 binds tubulin in two distinct regions. TAN1-tubulin binding may potentially sequester TAN1 both in dynamic microtubule assays and in vivo. Alternatively, TAN1-tubulin binding may promote microtubule rescue, similar to Clasp (Al-Bassam et al., 2010). Further experiments would need to be performed to determine whether TAN1 dimerizes or multimerizes, whether tubulin-binding occurs in vivo, whether tubulin and microtubule binding sites overlap, and their relative affinities.

Abnormal cell shape is likely responsible for spatial positioning defects of the PPB in the *tan1* mutant

Defects in division plane orientation can occur early in the cell cycle, before the formation of the PPB, or later, after the PPB has already formed. We showed using live-cell imaging that *tan1* mutant phragmoplasts did not return to the division site previously marked by the PPB, indicating a later defect in division plane orientation (Martinez et al., 2017). In contrast, previous work indicated that the orientation of the PPB is more variable in *tan1* mutant compared to wild-type cells, indicative of a potential PPB placement defect (Cleary and Smith, 1998; Mir et al., 2018). However, whether TAN1 contributes to proper PPB placement is unclear because TAN1 protein does not accumulate at the division site until late G2, after the PPB has already formed (Martinez et al 2017).

Previous measurements of PPB placement were obtained from 2D micrographs which might not accurately reflect the position of the PPB in 3D, particularly in cells with irregular shapes. To overcome this shortcoming, we used our recently developed mathematical modeling approach to accurately predict

3D division planes (Martinez et al., 2018). This model generates soap-film minima from real, 3D cell shapes and allows us to compare purely geometric predictions to in vivo cell division sites (Martinez et al., 2018). The majority of predicted divisions closely match in vivo animal and plant cell divisions (Martinez 2018). We collected confocal Z-stacks and used the image processing software MorphoGraphX (Barbier de Reuille et al., 2015) to extract wild-type (Figure 3A) and *tan1* mutant three-dimensional cell shapes (Figure 3B). We then used Surface Evolver to generate 3D reconstructions of the cells. Then, the gradient descent function in Surface Evolver was used to generate soap-film minima that divided the volume into two equal halves. These soap-film minima are division planes predictions (Martinez et al., 2018; Brakke, 1992). The predicted division planes were then compared to the in vivo PPB location (Figure 3A-B). To measure the offset between the predicted division and the location of the PPB, we compared the location of the midplane of the PPB to the outer edge of the predicted division. When the value of the PPB offset is low, the prediction matches the in vivo division plane. For wild-type cells, the average PPB offset from the predicted divisions was $0.40\mu m^2 \pm 0.96$ (average ± standard deviation (SD), n = 16), while PPB offset was higher in *tan1* mutants (PPB offset = $1.85\mu m^2 \pm 3.93$, average ± SD, n = 45; p-value = 0.0012 Mann-Whitney, Figure 3C).

To determine whether the increased PPB offset in *tan1* mutants is due to improper PPB placement or an indirect consequence of abnormal cell shapes in the *tan1* mutant, we developed a quantitative method to compare cell shapes called the "abnormality index" by measuring the distance between the surface area center and volume center (see Materials and Methods). Wild-type cells had about 3-fold lower and more consistent abnormality index compared to *tan1* mutant cells (Figure 3D, wild-type cells n = 16 abnormality index = 0.14 ± 0.1, *tan1* n = 45 abnormality index = 0.39 ± 0.35 p-value = < 0.0008 Mann-Whitney; average ± SD). These data confirm that wild-type plants tend to have normally shaped cells, while *tan1* mutants have cells with both normal and abnormal shapes, consistent with our imaging data.

If TAN1 plays a direct role in PPB placement, we would expect abnormal PPB placement in *tan1* mutants regardless of variations in cell shape abnormality index. In contrast, we found a significant positive correlation between abnormality index and PPB offset in *tan1* mutant cells (Spearman correlation coefficient = 0.59, p value = <0.0001, n = 45 cells), suggesting that PPB placement deviated from predicted divisions more in highly abnormally shaped cells. To address whether this trend was similar in wild-type cells, we specifically looked for and modeled additional wild-type cells which displayed aberrant cell shapes with high abnormality indices (Spearman correlation coefficient = 0.57, p value = 0.003 n = 25 cells). Both wild-type and *tan1* mutant cells with higher abnormality indices typically had higher PPB offsets for the whole dataset (Figure 3E, left panel) as well as the dataset removing outliers (Figure 3E, right panel), with examples of cells with high abnormality indices shown in (Figure 3F-J). Due to the correlation between PPB placement defects and aberrant cell shapes in *tan1* mutants, we hypothesize that defects in PPB placement are a consequence of cell shape abnormalities and not directly related to TAN1 function during G2.

Modeling approaches based on microtubule organization suggest that interphase cortical microtubule arrangements may be an important modulator in PPB positioning (Chakrabortty et al., 2018; Mirabet et al., 2018). The orientation of the PPB typically follows the orientation of the prior interphase microtubule array (Flanders et al., 1989; Gunning and Sammut, 1990). Our result suggests that intrinsically abnormally shaped cells may lead, in the next round of cell division, toward less geometrically accurately placed PPBs. This effect may explain why other division plane mutants have offset or oblique PPBs (Pietra et al., 2013; Müller et al., 2006a). Additionally, mutants with cell expansion defects that cause aberrant cell shapes may also lead first to misoriented PPBs and then apparent division plane defects.

Spindle organization is disrupted in the *tan1* mutant

Previously, we showed that *tan1* mutant cells had mitotic progression delays during metaphase and telophase, but we did not propose a specific hypothesis to explain why delays occurred (Martinez et al.,

2017). If TAN1 plays a significant role in crosslinking spindle microtubules, metaphase delays may reflect defective spindle organization. Using time-lapse imaging, we assessed overall spindle morphology in maize leaf cells expressing YFP-TUBULIN. In wild-type cells, we always observed bipolar spindles (n = 38) (Figure 4A). In *tan1* mutant cells, spindles occasionally displayed delayed bipolar organization (13.5% n = 5/35), but recovered after ~20 ± 8 minutes (average ± SD) following nuclear envelope breakdown into typical bipolar spindles (Figure 4B, Supplementary Movie 2). Metaphase delays previously described in *tan1* mutants occurred frequently, leading to an average 1.5x time delay compared to wild-type (Martinez et al., 2017), whereas delayed bipolar spindle organization defects were more rare. This suggests that defects in microtubule organization only occasionally lead to detectable defects in spindle organization in the *tan1* mutant, consistent with redundant mechanisms for spindle assembly. Metaphase spindle microtubules crosslinking or bundling is important for proper and timely spindle assembly (Masoud et al., 2013; Mullen and Wignall, 2017; Ambrose and Cyr, 2007; Winters et al., 2019). Based on in vitro microtubule zippering by TAN1, it is possible that TAN1 mediates bundling of spindle microtubules as they encounter each other at shallow angles. Thus, TAN1 localization to the spindle might be important for correct spindle assembly and mitotic progression through metaphase.

Microtubules and TAN1 co-localize at the division site during telophase

To understand how TAN1 might mediate phragmoplast guidance during telophase (Martinez et al., 2017; Mir et al., 2018), we imaged TAN1 and microtubules at the division site. CFP-TUBULIN labeled microtubules and TAN1-YFP were imaged together in cells undergoing longitudinal divisions, where phragmoplast guidance is more readily visualized. Colocalization of CFP-TUBULIN and TAN1-YFP at the division site was assessed at the cell cortex after initial phragmoplast contact. A small number of phragmoplast microtubules co-localize with TAN1 puncta (Pearson's correlation coefficient 0.23 ± 0.078 average ± SD, n = 21), but about half of the TAN1 puncta were associated with microtubules (Manders overlay coefficient, C = 0.41 ± 0.1 average ± SD, Figure 4C). Together, these results suggest that a small subpopulation of microtubules from the leading edge of the phragmoplast interact with cortical TAN1

puncta as the phragmoplast expands across the division site (Figure 4D-E, Supplemental Video 3). These TAN1 puncta at the division site do not appear to be mobile over imaging of about 5 minutes (n = 8 cells, Figure F-G).

Models for phragmoplast guidance previously proposed that leading edge phragmoplast microtubules interact with proteins at the cortical division site either through specific protein-protein interactions or microtubule-protein interactions (Herrmann et al., 2018; Lipka et al., 2014; Li et al., 2017). POK2, which is localized to the division site, was shown to be a plus-end directed kinesin (Chugh et al., 2018). POK2 may effectively push against the plus-ends of microtubules which encounter the division site (Chugh et al., 2018). POK2 also directly interacts with MAP65-3, which is localized to bundled microtubules both at the phragmoplast midzone and leading edge, serving as another potential type of interaction between the phragmoplast and the division site. The localization of TAN1 at the division site is important for its function in phragmoplast guidance (Mir et al., 2018; Martinez et al., 2017). Based on the results from this study, we propose that end-on interactions between the plus-ends of phragmoplast leading edge microtubules and TAN1-YFP puncta at the division site may exert pulling forces on these microtubules to guide phragmoplast trajectory.

While TAN1 has long been characterized as a microtubule binding protein, the functional significance of this finding remained elusive. Our in vitro analysis of TAN1-microtubule activities combined with live-imaging observations of TAN1 localization on spindle microtubules and at phragmoplast leading edge microtubule tips suggest that TAN1-microtubule interactions may depend on the geometry of microtubule encounters. This provides a plausible explanation for how TAN1 contributes to spindle organization and phragmoplast guidance.

Materials and Methods

HIS-TAN1 and HIS-TAN1-GFP purification and labeling

A codon-optimized cDNA encoding the maize HIS-TAN1 and HIS-TAN1-GFP was synthesized in vitro, followed by protein expression and purification, all performed by Genscript (Genscript Corp Piscataway, New Jersey USA). *E. coli* strain SHuffle was transformed with recombinant plasmid encoding HIS-TAN1. After cell pellets were sonicated and centrifuged, the precipitate was dissolved using urea, followed by affinity purification. *E. coli* strain BL21 Star (DE3) was transformed with recombinant plasmid encoding HIS-TAN1-GFP. After cell pellets were sonicated and centrifuged, the precipitate was dissolved using urea, followed by affinity purification (Genscript Corp Piscataway, New Jersey USA). Proteins were refolded and sterilized by filtering. HIS-TAN1 and HIS-TAN1-GFP concentrations were checked with a BCA protein assay (Genscript Corp Piscataway, New Jersey USA). After refolding, HIS-TAN1-GFP was no longer fluorescent. HIS-TAN1-GFP therefore was tagged with an Atto488 dye. HIS-TAN1-GFP was conjugated with Atto488-maleimide (Sigma 28562). 4µM HIS-TAN1-GFP in 80mM PIPES, 1mM MgCl2, 1mM EGTA buffer was reduced with 12.5µM Tris(2-carboxyethyl)phosphine hydrochloride for 10 minutes followed by a 4 hour incubation with 250µM Atto488 dissolved in DMSO (10mM) at room temperature. Unreacted excess dye was removed by running the sample through a 10DG desalting column (BioRad 732-2010) and concentrating with a 30K MWCO PES concentrator (Thermo 88521). HIS-TAN1-GFP and HIS-TAN1-GFP-Atto488 (~80% degree of labeling) activity was confirmed by microtubule co-sedimentation assay. Conjugation of Atto488 dye was determined by imaging the results of the microtubule cosedimentation assay on a SDS-PAGE experiment using a UV light source showing fluorescent bands corresponding to a Atto488 tagged HIS-TAN1-GFP.

Microtubule binding and co-sedimentation

A microtubule binding assay kit was used to assess HIS-TAN1 microtubule binding in relation to positive and negative controls, according to manufacturer conditions (Cytoskeleton Inc., MK029). For determining affinity of HIS-TAN1 to microtubules, microtubules were polymerized from 50µM starting concentration of tubulin in the presence of 1mM GTP for 2 hours at 37°C followed by the addition of 10µM taxol. HIS-TAN1 and microtubules were incubated for 25 minutes and spun down at 39,000 x *g* at

25°C. HIS-TAN1-GFP and HIS-TAN1-GFP-Atto488 protein was incubated with microtubules at room temperature for 25 minutes and spun down at 21,000 x *g* at 25°C. Equal volumes of soluble and pellet samples were loaded into an SDS PAGE (10% gel), and stained with Coomassie. The percent of TAN1 cosedimentation was determined by measuring the ratio between TAN1 protein found in the pellet over the total TAN1 protein found in both the pellet and soluble as determined by densitometry analysis using ImageJ Gel Analysis tool. Correction by subtracting TAN1 from the pellet fraction samples without microtubules, was applied to spindowns due to some TAN1 precipitation during the assay in samples without microtubules. Spindowns were performed at least three times for each concentration tested. Curve-fitting and statistical analysis was performed using MATLAB and GraphPad Prism. Figure construction) was performed using GraphPad Prism. To assess microtubule binding by microscopy, rhodamine labeled microtubules (1:25 rhodamine tubulin:unlabeled tubulin) were polymerized from 50μM starting concentration of tubulin in the presence of 1mM GTP for 2 hours at 37°C followed by the addition of 10μM taxol. 100nM rhodamine labelled microtubules were incubated with 50nM HIS-TAN1-Atto488 for 5 minutes and then pipetted onto a coverslip and imaged. Timelapse analysis was performed using 1μM rhodamine labeled GMPCPP stabilized microtubules (1:25 rhodamine tubulin:unlabeled tubulin) incubated with 1nM HIS-TAN1-Atto488 for 10 minutes then imaged at 1 or 2 second intervals.

Transient expression in *Nicotiana benthamiana*

5 week-old *N. benthamiana* plants grown under standard 16-hour light, 8-hour dark conditions were used for transient co-localization experiments. Plasmids for constitutively expressing the viral protein p19, RFP-TUBULIN6 (Ambrose et al., 2011) and TAN1-GFP (Walker *et al.,* 2007) were transformed into *Agrobacterium tumefaciens* strain GV3101. Agrobacteria were grown to stationary phase, spun down at 1000 rpm, then resuspended for one hour at room temperature in infiltration buffer containing 10 mM MES (pH 5.7), 10 mM MgCl2, 0.5% D-glucose (w/v), and 200 μM acetosyringone. Equal amounts of Agrobacteria (with and without the TAN1-GFP) were mixed together and a 1 ml syringe without a needle was used to infiltrate the abaxial side of *N. benthamiana* leaves. After three days of incubation, the leaves

were removed, the abaxial epidermal cells were imaged using the spinning confocal disk microscope with the 60X objective described above. Maximum intensity projections and automatic background subtraction in FIJI were used in Supplemental Figure 2.

Reconstitution of in vitro microtubule dynamics

In-vitro microtubule dynamics were conducted according to previous protocols (Dixit and Ross, 2010). Flow chambers were assembled using silanized coverslips and double-sided sticky tape with a chamber volume of ~20μL. A 20% monoclonal anti-biotin antibody (clone BN-34, Sigma, St. Louis, MO) was used to coat the surface followed by blocking with 5% pluronic F-127 (Sigma #P2443) for five minutes each step. Rhodamine and biotinylated guanosine-5′-(α,β-methylene)triphosphate (GMPCPP) microtubule seeds were then flowed into the cell. Microtubule growth was initiated using 17.5μM 1:25 rhodamine-labeled bovine tubulin in 80mM PIPES, 1mM MgCl2, 1mM EGTA with 0.15% methylcellulose (w/v), 100mM DTT, oxygen scavengers (250μg/mL glucose oxidase, 25μg/mL catalase), 5mg/mL glucose, 2mM GTP along with the specified amount of HIS-TAN1 protein. To assess microtubule bundling, a higher concentration of tubulin (22.5μM, 1:25 rhodamine tubulin:unlabeled tubulin) was used in the reaction to promote microtubule growth and crossovers. At least two slides were prepared for each concentration and experimental condition. The samples were excited with a 561-nm (at 4 mW output) diode-pumped solid-state laser (Melles Griot, Albuquerque, NM) and visualized through a 100X objective (NA 1.45) and back-illuminated electron-multiplying CCD camera with a 582-636nm emission filter set using TIRF (ImageEM, Hammamatsu). Images were collected every 2 seconds. Kymographs were used to analyze data in FIJI (Schindelin et al., 2012).

In vitro pulldown of HIS-TAN1-GFP and tubulin

10 μL of agarose beads bound to anti-GFP (MBL D153-8) were incubated with 500 nM HIS-TAN1-GFP (for calculation of stoichiometry) or 1 μM HIS-TAN1-GFP (for determining ability to pull down tubulin) or 1μM HIS-GFP (ABM 00033P) and 5 μM of TUBULIN (Cytoskeleton T240) in BRB80 buffer with 50

mM NaCl, 0.2 mM PMSF, 10 mM DTT, 0.05% Tween-20. Samples were incubated for three hours at 4°C and subsequently washed three times using BRB80 supplemented with 50 mM NaCl and 0.05% Tween-20. Beads were then transferred to a new tube and washed four more times with BRB-80 supplemented with 50 mM NaCl and 0.05% Tween-20. Coomassie stained SDS-PAGE was used for protein visualization and analyzed by densitometry using ImageJ to determine protein amounts which were pulled down.

Size exclusion chromatography

Molecular weight standards were prepared according to manufacture specifications, except they were resuspended in BRB80 buffer (Sigma MWGF1000). Equal sample volume of standard was run twice on a Superdex 200 Increase 10/300 GL column (GE Lifesciences) using an NGC Chromatography System (2mL injection volume, 0.25 mL/min flow rate, Bio-Rad) with absorbance at 280nm recorded during the experiment (Supplemental Figure 3B). Blue Dextran (Sigma MWGF1000) was used to determine void volume of the column. A semilog plot of elution volume over void volume for each standard versus molecular weight was constructed to calculate a standard curve to determine tubulin molecular weight (GraphPad Prism 8.4) (Supplemental Figure 3C). Equal volume of 1 mg/mL (10μm) and 0.5mg/mL (5 μm) tubulin (Cytoskeleton T240) in BRB80 buffer was run on column to determine likely oligomerization state of tubulin used for experiments.

Predicting Division Planes from Wild-Type and *tan1* Cell Shapes using Surface Evolver

Samples from WT and *tan1* mutant maize plants expressing YFP-TUBULIN (α-tubulin fused to the Citrine variant of Yellow Fluorescent Protein, (Mohanty et al., 2009)) were dissected to the symmetrically dividing leaf zones to identify PPB location. To identify the cell outlines for three-dimensional reconstruction, samples were either stained with 0.1mM propidium iodide or expressed PLASMA MEMBRANE INTRINSIC PROTEIN2-1 fused to CFP to outline the plasma membranes (Mohanty et al., 2009). Three-dimensional cell shape reconstructions were generated using MorphoGraphX, while three-

dimensional PPB reconstructions were generated using Trainable Weka Segmentation (Barbier de Reuille et al., 2015; Arganda-Carreras et al., 2017). Cells were collected from more than three individual plants for each genotype. A previous protocol was followed for modeling symmetric divisions by soap-film minimization using Surface Evolver (Brakke, 1992; Martinez et al., 2018). This model generates soap-film minima from real, 3D cell shapes to explicitly test the hypothesis that plant cell divisions mimic mathematically predicted soap-film minima (Errera 1888). As we previously demonstrated for both plant and animal cells, the majority of predicted divisions closely match in vivo divisions (Martinez 2018). This model does not take into account cell-cell interactions, mechanical or developmental cues. Briefly, cell outlines were smoothed using 30th degree spherical harmonics followed by surface area minimization from 241 starting planes with normals uniformly distributed over a sphere. For PPB offset measurements, the distance between the midplane of the PPB and the surface of the predicted division was measured in microns squared. Abnormality index was defined by the distance between the area surface center and the volume center for the cell. The Surface Evolver pipeline can be downloaded from Github (https://github.com/jdhayes/predictive_division/).

Colocalization analysis

Maize plants were dissected to reveal the symmetrically dividing leaf zones to image TAN1-YFP and CFP-TUBULIN at the cortex of maize epidermal cells during telophase using a Zeiss 880 LSM. Airyscan super resolution mode was used and the images were processed using default settings. Three separate plants were imaged for the collection of cells. Micrographs were imported into FIJI and cropped to the cell of interest where colocalization was assessed. Just Another Colocalization Plugin (JACoP) was used in order to determine the Pearson Correlation Coefficient and Manders Overlap Coefficient for each cell (Bolte and Cordelières, 2006). Data generated was analyzed using GraphPad (Prism).

Microscopy for in vitro and in vivo imaging

Taxol stabilized rhodamine labeled microtubules and HIS-TAN1-GFP-Atto488 were visualized on an inverted Nikon Ti stand (Nikon) with a W1 spinning disk (Yokogawa) and a motorized stage (ASI Piezo) run with Micromanager software (micromanager.org) and built by Solamere Technology. Time-lapse of rhodamine labeled GMPCPP stabilized microtubules and HIS-TAN1-Atto488 was also imaged on this microscope. Solid-state lasers (Obis) and emission filters (Chroma Technology) used had excitation 561 nm; emission, 620/60 nm (for rhodamine-tubulin); and excitation, 488 nm; emission, 520/50 nm(for HIS-TAN1-GFP-Atto488). A 100x oil lens (1.45 numerical aperture) and Immersion Oil Type FF (Cargille immersion oil, 16212) was used. Maize epidermal cells used for modeling were visualized using a 60× water-immersion objectives with 1.2 numerical aperture. An excitation of 561; emission, 620/60 (for propidium iodide) and excitation of 514; emission, 540/30 (for YFP-TUBULIN). Perfluorocarbon immersion liquid (RIAAA-678; Cargille) was used on the objective.

Dynamic rhodamine-labeled microtubules were excited with a 561-nm (at 4 mW output) diode-pumped solid-state laser (Melles Griot, Albuquerque, NM) using a 100X (NA 1.45) objective and TIRF microscopy, described above. Images were acquired with a back-illuminated electron-multiplying CCD camera (Hamamatsu, Bridgewater, NJ, ImageEM) and rhodamine filter sets (582–636 nm emission).

Colocalization data on TAN1-YFP and CFP-TUBULIN in Figure 4 was collected using a Zeiss LSM 880 Elyra, Axio Observer and a 100x/1.46 NA Oil lens (Cargille immersion oil, 16212). TAN1-YFP was excited with 514 while CFP-TUBULIN was excited using 458 and imaged using super resolution airyscan mode with a MBS 458/514 and 420-480 BP + LP 605 filter set. Airyscan images were processed using default settings using Zen Black software (Zeiss).

Supplemental Material

Supplemental Figure 1 shows HIS-TAN1-GFP and HIS-TAN1-GFP-Atto488 microtubule binding and affinity using quantitative microtubule co-sedimentation assay.

Supplemental Figure 2 shows colocalization of TAN1 and cortical microtubules in *Nicotiana benthamiana* (tobacco).

Supplemental Figure 3 shows HIS-TAN1-GFP and tubulin pulldown, and confirmation of tubulin dimerization by size exclusion chromatography.

Supplemental Movie 1 shows HIS-TAN1 mediated microtubule crosslinking events observed during in vitro dynamic microtubule reconstitution assays imaged using TIRF microscopy.

Supplemental Move 2 displays examples of spindle organization of wild-type (left) and two *tan1* mutant cells as they progress through mitosis.

Supplemental Movie 3 shows potential microtubule interactions between the phragmoplast leading edge and TAN1-YFP protein localized at the cortical division site in maize epidermal leaf cells.

Acknowledgements

Thanks to Ms. Jocelyne Aranda, Mr. Christopher Hoyt, and Ms. Sukhmani Sidhu for collecting some images used for the modeling work presented. Thanks to Dr. Hong Liang for help with transient tobacco assays. We thank Dr. David Carter (University of California, Riverside) for Zeiss LSM 880 training. We thank Prof. Laurie Smith (University of California, San Diego) for the TAN1-GFP plasmid and Prof. Chris Ambrose (University of Saskatchewan) for the RFP-TUBULIN plasmid. We also thank the University of California, Riverside Agricultural Operations (AgOps) for greenhouse and field space, and David Wetovick (AgOps) for helpful field management. Funding from NSF-MCB1716972 and USDA-NIFA to CGR and from NSF-MCB1453726 to RD is gratefully acknowledged. Funding from a Ford Foundation Dissertation Fellowship to PM is gratefully acknowledged.

Author contributions

CGR, RD, AZ, SEO'L and KAB provided equipment, reagents and experimental guidance. PM and RB performed in-vitro experiments with RB offering assistance on microtubule co-sedimentation. PM captured images used for modeling and performed live cell time-lapse. PM and AZ performed size exclusion chromatography. CGR, SEO'L and RD supervised experiments. PM and CR analyzed data and made figures, PM and CGR wrote manuscript with comments and edits from coauthors. CGR, PM and RD acquired funding.

Plus-end dynamics	0 µM HIS-TAN1	0.1 µM HIS-TAN1	0.5 µM HIS-TAN1	1 µM HIS-TAN1	2 µM HIS-TAN1
Growth events (n)	156	180	166	214	196
Growth Rate (µm/sec, mean +/- S.D.)	1.8 ± 0.4	1.8 ± 0.3	1.8 ± 0.3	*1.7 ± 0.5	***1.5 ± 0.3
Shrinkage events (n)	109	127	113	153	149
Shrinkage Rate (µm/sec, mean +/- S.D.)	31.5 ± 15.6	27.7 ± 10.8	*26.2 ±8.8	27.8 ± 9.7	***24.2 ± 10.0
Time growing (%)	94.9	93.8	94.5	94.6	95.2
Time shrinking (%)	5.1	**6.2	*5.5	5.4	4.8
Catastrophe Frequency (events/minute)	0.3	0.4	0.4	0.4	0.5
Crossovers (n)	445	346	334	334	506
Bundling events (n)	2	0	0	3	139
Bundling frequency (%)	0.5	0	0	0.9	27.5

Table 1: Summary of microtubule dynamics and microtubule interactions at different concentrations of HIS-TAN1. Bundling includes both zippering and pulling. Significance was calculated by comparing values to 0µM HIS-TAN1 determined by Mann-Whitney test indicated by (*) p-value > 0.05, (**) p-value > 0.01, (***) p-value > 0.001. Three trials were performed for each concentration of HIS-TAN1.

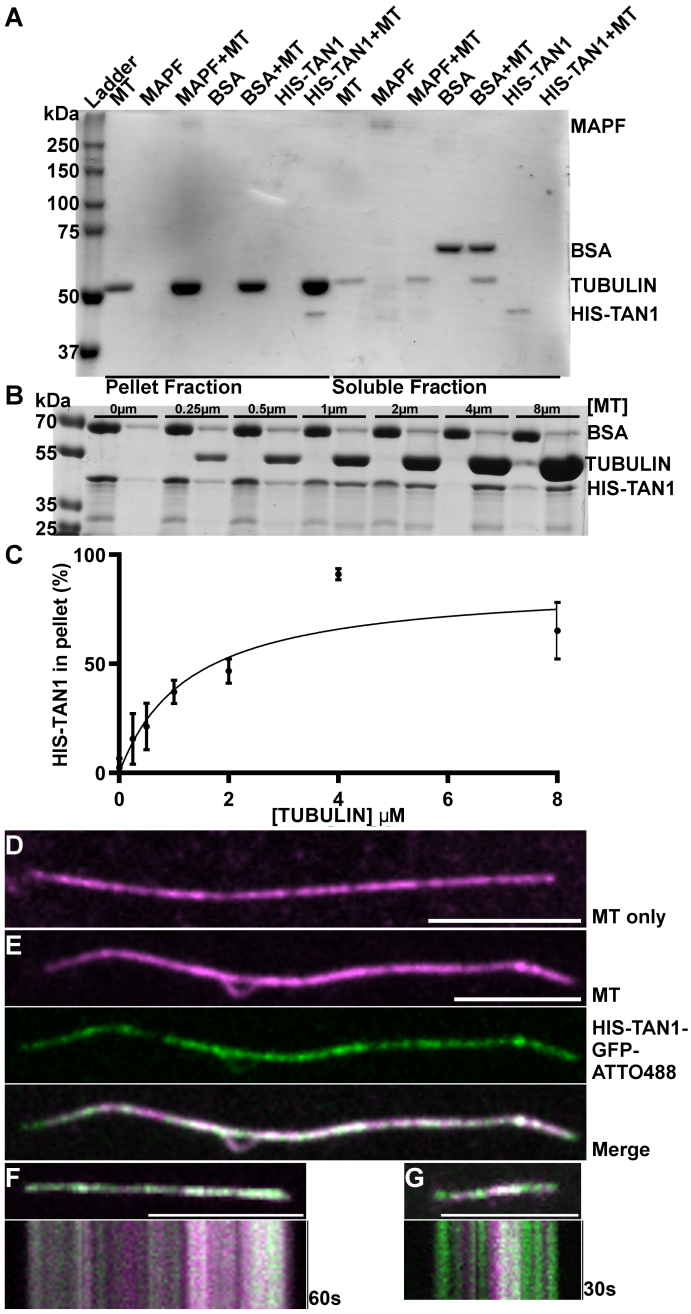

Figure 1: Recombinantly expressed TAN1 binds to microtubules. (A) Coomassie stained SDS PAGE results from microtubule cosedimentation with HIS-TAN1, positive control (MAPF, 70% MAP2) and negative control (BSA) controls separated into corresponding pellet and soluble fractions. (B) Coomassie stained SDS PAGE results from microtubule cosedimentation assay using 2µM HIS-TAN1 and from 0-8µM of tubulin. (C) Hyperbolic fit of microtubule cosedimentation data for HIS-TAN1 at varying concentrations of microtubules determines an apparent $K_{0.5}$ value of 1.08 µM (95% CIs: 0.722 to 1.43 µM), removing the outlier at 4 µM tubulin (D, E) Rhodamine-labeled, taxol-stabilized microtubule in buffer only control (magenta) (D) or incubated with HIS-TAN1-GFP-Atto488 (green). (F-G) Time-lapse and kymograph of rhodamine labeled GMPCPP stabilized microtubules (magenta) and HIS-TAN1-GFP-Atto488 (green). Scale bar is 10 µm.

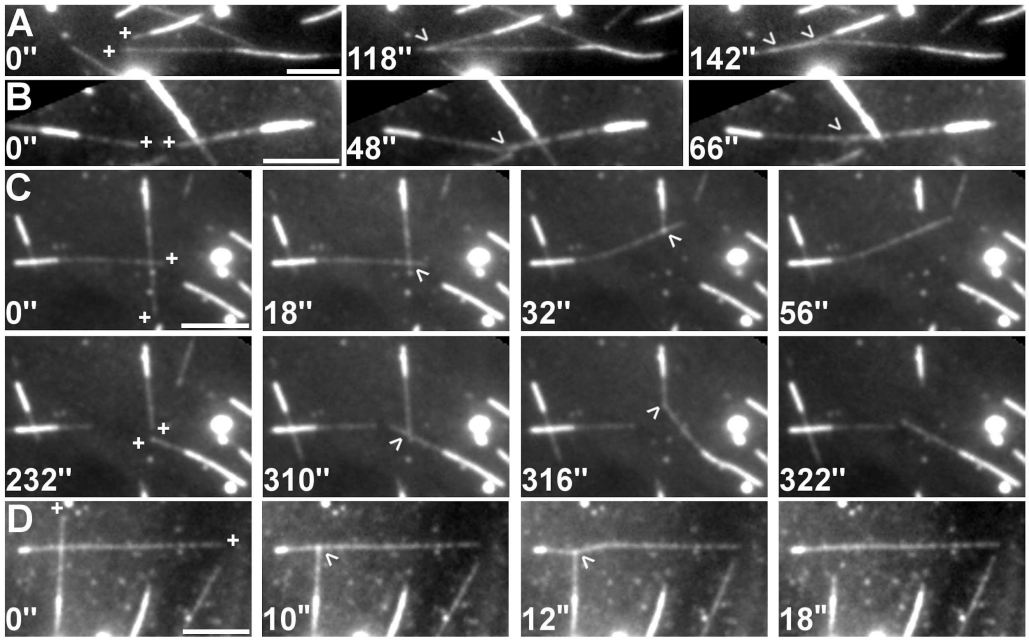

Figure 2: HIS-TAN1 contact-angle-independent dynamic microtubule interactions. (A-D) Dynamic rhodamine-labelled microtubules nucleated from GMPCPP-stabilized seeds with plus-ends indicated by a (+) and a crossover indicated with an arrowhead. Microtubule seeds are identified by their brighter signal compared to the growing microtubule ends. 2μM HIS-TAN1 is present in the assay. (A) Two microtubule plus-ends are indicated with their plus-ends polymerizing in the same direction. These microtubules encounter each other in a parallel orientation and are zippered together. (B) Two microtubule plus-ends are indicated with their plus-ends growing towards each other. These microtubules are zippered together in an antiparallel orientation. (C) Two microtubule plus-ends are indicated at the start (0"). These microtubules crossover and at 18" one of them depolymerizes. The depolymerizing end of this microtubule appears to pull on the other microtubule over the course of depolymerization. At 232" (new plus-end growth indicated) a new crossover is formed followed by a depolymerization event which again pulls at the crossover with the non-depolymerizing microtubule (316"). Timelapse shown in Supplemental Video 1. (D) Two microtubule plus-ends are indicated at the start (0") which cross over at a high angle (~90°). Depolymerization of one microtubule leads to transient deformation of the other microtubule at the crossover point. Scale bar is 10 μm.

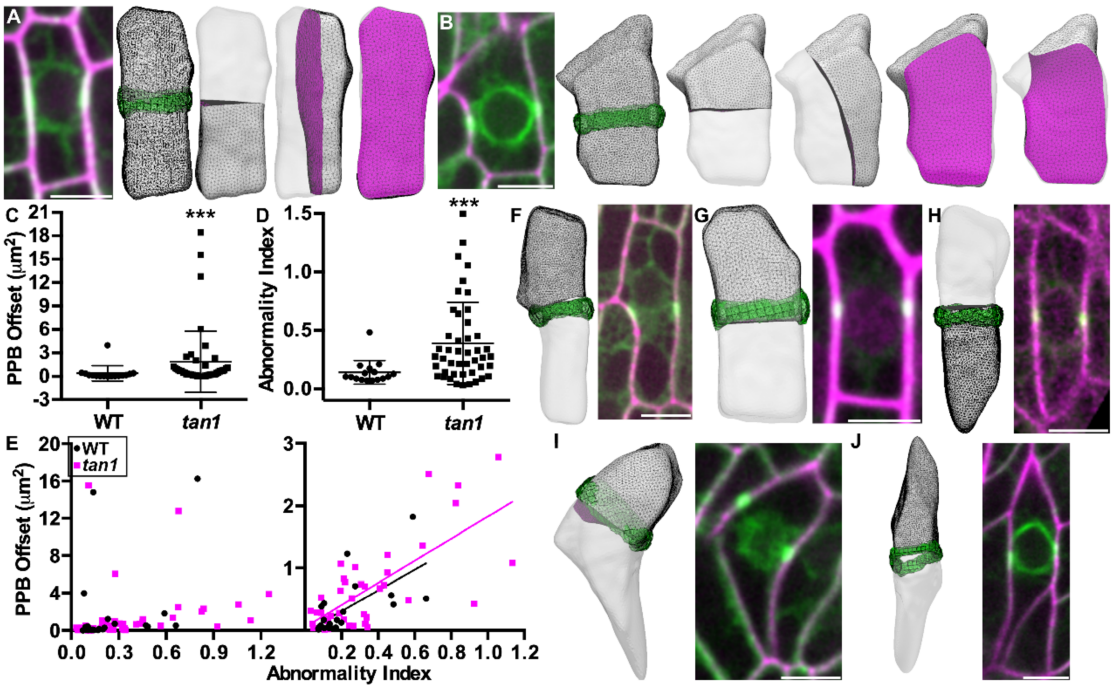

Figure 3: Abnormally shaped cells have higher PPB offset in wild-type and *tan1* cells.
(A) On the left is a micrograph of wild-type maize leaf epidermal cell expressing YFP-TUBULIN (green) stained with propidium iodide (magenta) next to the 3D cell shape reconstruction generated with Surface Evolver (grey mesh). The green band is the 3D reconstruction of the PPB. Predicted soap-film minimum divisions for the cell are shown with magenta meshes, from left to right transverse, longitudinal, periclinal division planes. B) Micrograph of *tan1* maize leaf epidermal cell next to cell shape reconstruction with PPB overlaid and (from left to right) transverse, longitudinal, periclinal and other division planes. (C) PPB offset in *tan1* mutants is significantly higher than WT (WT n = 16 PPB offset = 0.40μm^2 ± 0.96, *tan1* n = 45 1.85μm^2 ± 3.93, average ± S.D.; p-value = 0.0012 (Mann-Whitney). (D) Abnormality index in *tan1* mutants is significantly higher compared to WT (WT n = 16 abnormality index is 0.14 ± 0.1, *tan1* n = 45 abnormality index is 0.37 ± 0.32 p-value < 0.0008 Mann-Whitney; Average ± S.D.) (E) Abnormality index versus PPB offset suggests abnormal cell shapes generally show higher offsets, WT r = 0.57, p value = .007 and *tan1* r = 0.59, p value <0.0001 (Spearman correlation coefficient). A subset of data (values of PPB offset < 3) is displayed adjacent with a linear fit of WT r = 0.7, p value = 0.0003, n = 22 and *tan1* r = 0.6, p value = < 0.0001, n = 40 (Spearman correlation coefficient). (F-J) Best-fit predicted divisions overlaid with in vivo PPB location next to corresponding micrograph of maize epidermal cells expressing YFP-TUBULIN (green) and either expressing membrane marker PIP2-CFP (H, magenta) or stained with propidium iodide (F-G, I-J, magenta) to outline the cell shape. (F) Example of a wild-type cell with abnormality index of 0.59 and PPB offset of 1.82μm^2. (G) Example of a wild-type cell with abnormality index of 0.09 and PPB offset of 0.39μm^2. (H) Example of a *tan1* mutant cell with abnormality index of 0.32 and PPB offset of 0.26μm^2. (I) Example of a *tan1* mutant cell with abnormality index of 1.25 and PPB offset of 3.92μm^2. (J) Example *tan1* mutant cell with abnormality index of 1.14 and PPB offset of 1.08μm^2. Scale bar is 10 μm.

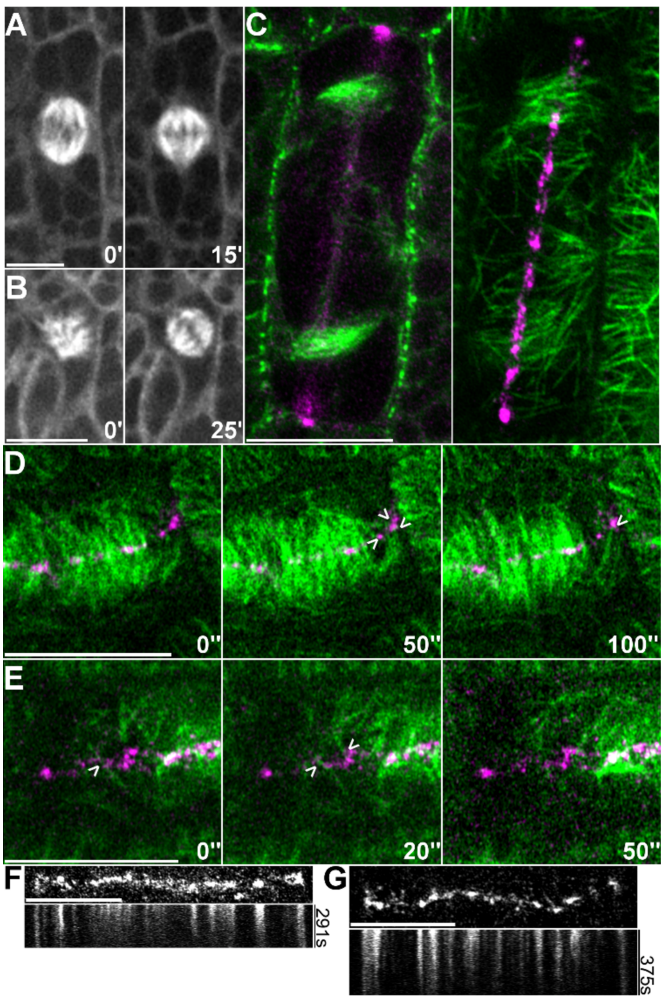

Figure 4: TAN1-mediated microtubule interactions may organize spindles and promote proper phragmoplast guidance.

(A) Wild-type maize epidermal cell expressing YFP-TUBULIN displays normal bipolar spindle morphology over time. (B) *tan1* maize epidermal cell expressing YFP-TUBULIN has a disorganized spindle that recovers to canonical bipolar organization. Time-lapse of spindles shown in Supplemental Video 2. (C-D) Wild-type maize epidermal cells expressing CFP-TUBULIN (green) and TAN1-YFP (magenta). (C) Micrographs display both at the midplane and cortex of cell undergoing a longitudinal division. Phragmoplast and leading-edge microtubules at the cortex are positioned at the division site and are partially colocalized with TAN1. (D-E) Time-lapse showing potential phragmoplast leading edge microtubule contact and interaction with TAN1 at the division site (arrowheads). Figure 4D is shown in Supplemental Video 3. (F-G) Time-lapse and kymograph of TAN1-YFP at the division site. Scale bar is 10 μm.

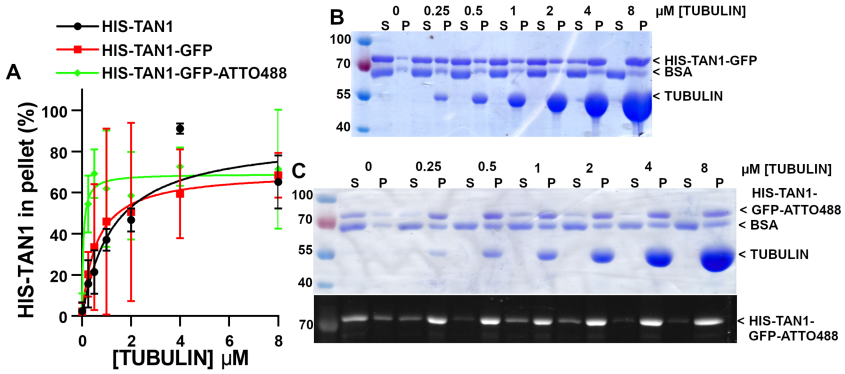

Supplemental Figure 1. HIS-TAN1-GFP and HIS-TAN1-GFP-Atto488 binding affinity to taxol stabilized microtubules. (A) HIS-TAN1-GFP Co-sedimentation binding data with fits to hyperbolic binding isotherms for HIS-TAN1 (replotted from Figure 1C), HIS-TAN1-GFP, and HIS-TAN1-GFP-Atto488. Apparent affinity for HIS-TAN1-GFP is 0.595 µM ± 0.389 to 0.800 µM, while HIS-TAN1-GFP-Atto488 is 0.05 µM ± 0.0009 to 0.129 µM corrected for the average pelleting in samples without microtubules added (average ± 95% CI). (B) Coomassie stained SDS PAGE experiment from spindown of HIS-TAN1-GFP in the presence of varying concentrations of tubulin (0-8 µM). (C) Coomassie stained SDS PAGE experiment from spindown of HIS-TAN1-GFP-Atto488 in the presence of varying concentrations of tubulin (0-8µM). Below Coomassie stained SDS-PAGE experiment, HIS-TAN1-GFP-Atto488 was excited using ultraviolet light source to confirm Atto488 maleimide conjugation with HIS-TAN1-GFP used in the spin-down assays.

Protein	Model	$K_{0.5}$ (μM)	95% CI ($K_{0.5}$)		n_H	95% CI (n_H)		RMSE	Residuals
			Lower	Upper		Lower	Upper		
HIS-TAN1	Hill – all protein active	1.96	1.58	2.34	0.669	0.502	0.835	0.0301	+
	Hill – 76% (52,100) active	1.16	0.273	2.04	0.940	0.418	1.46	0.0246	+
	Hyperbolic – all active	2.25	1.23	3.26				0.0712	–
	Hyperbolic – 74% (65,82) active	1.08	0.721	1.434				0.0217	+
	Quadratic – all active	2.24	0.0550	4.42				0.0796	–
	Quadratic – 74% (52,95) active	0.736	0.524	0.948				0.0251	+
TAN1-GFP	Hill – all active	1.42	1.2	1.64	0.562	0.432	0.692	0.0305	+
	Hill – 76% (54,97) active	0.753	0.105	1.4	0.836	0.332	1.34	0.0272	+
	Hyperbolic	1.73	0.853	2.61				0.0983	–
	Hyperbolic – 70% (64,77) active	0.595	0.389	0.800				0.0263	+
	Quadratic – all active	1.73	-0.956	4.42				0.108	–
	Quadratic – 70% (59,82) active	0.600	-0.263	1.462				0.0294	+

Supplemental Table 1. Model fitting for TAN1–microtubule binding data. Fitted parameters and goodness-of-fit metrics for different TAN1–microtubule binding models, determined by curve fitting in MATLAB. $K_{0.5}$ reflects the concentration at which half-maximal binding is attained. Fitted expressions for fractional binding were: (1) Hill: $[T]^n/(K_{0.5}^n + [T]^n)$; Hyperbolic: $\left(\frac{[T]}{K_{0.5}+[T]}\right)$; Quadratic: $[K_{0.5} + [N]_0 + [T]_0 - \sqrt{(K_{0.5} + [N]_0 + [T]_0)^2 - 4[N]_0[T]_0}]/2[N]_0$, with $[T]$ and $[N]$ representing the tubulin and TAN1 concentrations, respectively. These expressions assume approach to 100% saturation of binding. Values are also given for models where the high-concentration asymptote was fitted as a parameter that multiplies each of these expressions, to account for a potential inactive protein fraction. The fitted active percentages of the protein are given in the "Model" column for these fits, followed by 95% confidence intervals for the percentages. The quadratic model fits $[N]_0 < \sim 10^{-5}$ μM in each case, which reduces statistical confidence in this model. In the Residuals column, '–' and '+' denote fits where clear nonrandom

trends in residuals were and were not observed, respectively. Note: HIS-TAN1-GFP-Atto488 fits are not provided here, as there were too few data points to properly describe the curvature in the binding data.

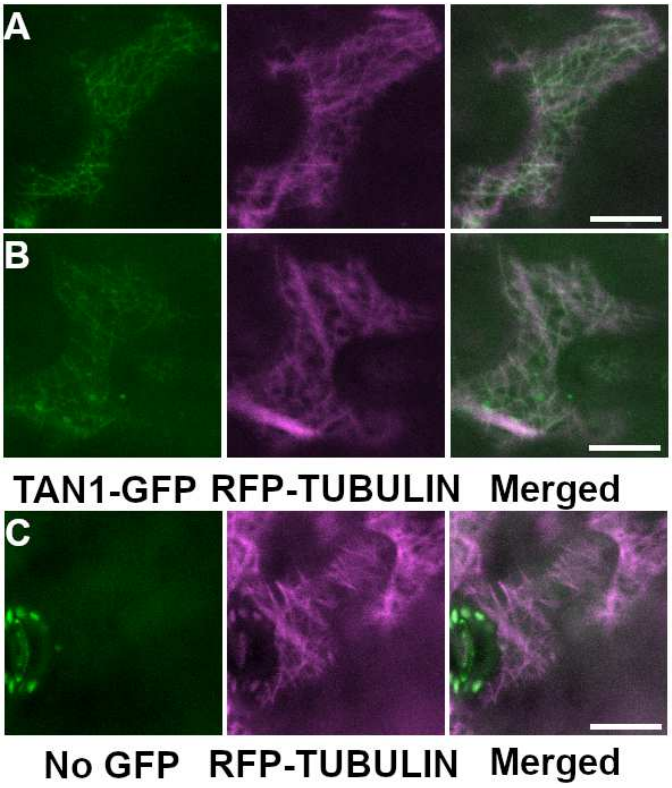

Supplemental Figure 2. Colocalization of TAN1 and cortical microtubules in *Nicotiana benthamiana* (tobacco) (A) and (B) TAN1-GFP (green) and RFP-TUBULIN labeled microtubules (magenta) co-localize (merged image) when expressed transiently in tobacco epidermal cells. (C) RFP-TUBULIN only expressed transiently in tobacco cells. Scale bar is 20 μm. Bright oval signals in guard cells in (C) are chloroplast autofluorescence.

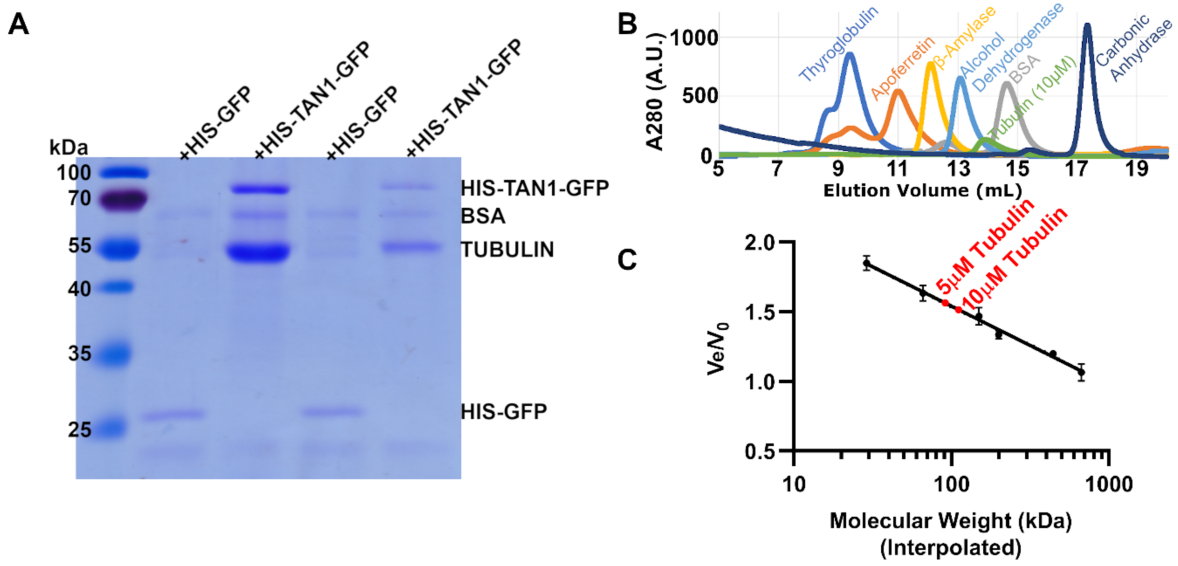

Supplemental Figure 3. HIS-TAN1-GFP binds to soluble tubulin dimers. (A) Agarose beads fused with an anti-GFP antibody were used to pull down HIS-TAN1-GFP or HIS-GFP in the presence of tubulin dimers. A tubulin band is detected after pulldowns in the presence of HIS-TAN1-GFP (1 μM) and not detected in the pulldown with HIS-GFP (1 μM). Coomassie-stained SDS-PAGE results from 2 independent in-vitro pull down are shown. Band intensity differences reflect differences in the relative amount of immunoprecipitated HIS-TAN1-GFP between experiments. (B) Size exclusion chromatography of one representative replicate of molecular weight standards and tubulin using FPLC. The A_{280} (A.U.) for each standard and tubulin was plotted against elution volume (V_e) for the same running conditions to determine the V_e for each protein. (C) Interpolated molecular weights for tubulin were plotted on a semilog V_e/V_0 curve determined from molecular weight standards (void volume determined by running blue dextran through column). Two replicates for 5 μM tubulin (91.45 kDa ± 12.32 kDa average ± SD) and 10 μM tubulin (111.13 kDa ± 14.18 kDa) and protein standards were run indicating that tubulin elutes as a dimer.

References

Al-Bassam, J., H. Kim, G. Brouhard, A. van Oijen, S.C. Harrison, and F. Chang. 2010. CLASP promotes microtubule rescue by recruiting tubulin dimers to the microtubule. *Dev. Cell*. 19:245–258.

Ambrose, C., J.F. Allard, E.N. Cytrynbaum, and G.O. Wasteneys. 2011. A CLASP-modulated cell edge barrier mechanism drives cell-wide cortical microtubule organization in Arabidopsis. *Nat. Commun.* 2:430.

Ambrose, J.C., and R. Cyr. 2007. The kinesin ATK5 functions in early spindle assembly in Arabidopsis. *Plant Cell*. 19:226–236.

Ambrose, J.C., and R. Cyr. 2008. Mitotic spindle organization by the preprophase band. *Mol. Plant*. 1:950–960.

Barbier de Reuille, P., A.-L. Routier-Kierzkowska, D. Kierzkowski, G.W. Bassel, T. Schüpbach, G. Tauriello, N. Bajpai, S. Strauss, A. Weber, A. Kiss, A. Burian, H. Hofhuis, A. Sapala, M.

711 Lipowczan, M.B. Heimlicher, S. Robinson, E.M. Bayer, K. Basler, P. Koumoutsakos, A.H.K.
712 Roeder, T. Aegerter-Wilmsen, N. Nakayama, M. Tsiantis, A. Hay, D. Kwiatkowska, I. Xenarios, C.
713 Kuhlemeier, and R.S. Smith. 2015. MorphoGraphX: A platform for quantifying morphogenesis in
714 4D. *Elife*. 4:05864.

715 Baskin, T.I., G.T.S. Beemster, J.E. Judy-March, and F. Marga. 2004. Disorganization of cortical
716 microtubules stimulates tangential expansion and reduces the uniformity of cellulose microfibril
717 alignment among cells in the root of Arabidopsis. *Plant Physiol.* 135:2279–2290.

718 Bolte, S., and F.P. Cordelières. 2006. A guided tour into subcellular colocalization analysis in light
719 microscopy. *J. Microsc.* 224:213–232.

720 Brakke, K.A. 1992. The Surface Evolver. *Exp. Math.* 1:141–165.

721 Burkart, G.M., and R. Dixit. 2019. Microtubule bundling by MAP65-1 protects against severing by
722 inhibiting the binding of katanin. *Mol. Biol. Cell*. mbcE18120776.

723 Buschmann, H., J. Dols, S. Kopischke, E.J. Peña, M.A. Andrade-Navarro, M. Heinlein, D.B. Szymanski,
724 S. Zachgo, J.H. Doonan, and C.W. Lloyd. 2015. Arabidopsis KCBP interacts with AIR9 but stays in
725 the cortical division zone throughout mitosis via its MyTH4-FERM domain. *J. Cell Sci.* 128:2033–
726 2046.

727 Chakrabortty, B., I. Blilou, B. Scheres, and B.M. Mulder. 2018. A computational framework for cortical
728 microtubule dynamics in realistically shaped plant cells. *PLoS Comput. Biol.* 14:e1005959.

729 Chan, J., G. Calder, S. Fox, and C. Lloyd. 2005. Localization of the microtubule end binding protein EB1
730 reveals alternative pathways of spindle development in Arabidopsis suspension cells. *Plant Cell*.
731 17:1737–1748.

732 Chugh, M., M. Reißner, M. Bugiel, E. Lipka, A. Herrmann, B. Roy, S. Müller, and E. Schäffer. 2018.
733 Phragmoplast Orienting Kinesin 2 Is a Weak Motor Switching between Processive and Diffusive
734 Modes. *Biophys. J.* 115:375–385.

735 Cleary, A.L., and L.G. Smith. 1998. The Tangled1 gene is required for spatial control of cytoskeletal
736 arrays associated with cell division during maize leaf development. *Plant Cell*. 10:1875–1888.

737 Dixit, R., and R. Cyr. 2004. Encounters between dynamic cortical microtubules promote ordering of the
738 cortical array through angle-dependent modifications of microtubule behavior. *Plant Cell*. 16:3274–
739 3284.

740 Dogterom, M., J.W.J. Kerssemakers, G. Romet-Lemonne, and M.E. Janson. 2005. Force generation by
741 dynamic microtubules. *Current Opinion in Cell Biology*. 17:67–74. doi:10.1016/j.ceb.2004.12.011.

742 Drechsler, H., Y. Xu, V.F. Geyer, Y. Zhang, and S. Diez. 2019. Multivalent electrostatic microtubule
743 interactions of synthetic peptides are sufficient to mimic advanced MAP-like behavior. *Mol. Biol.*
744 *Cell*. 30:2953–2968.

745 Drevensek, S., M. Goussot, Y. Duroc, A. Christodoulidou, S. Steyaert, E. Schaefer, E. Duvernois, O.
746 Grandjean, M. Vantard, D. Bouchez, and M. Pastuglia. 2012. The Arabidopsis TRM1-TON1
747 interaction reveals a recruitment network common to plant cortical microtubule arrays and
748 eukaryotic centrosomes. *Plant Cell*. 24:178–191.

749 Ehrhardt, D.W., and S.L. Shaw. 2006. MICROTUBULE DYNAMICS AND ORGANIZATION IN THE

PLANT CORTICAL ARRAY. *Annual Review of Plant Biology*. 57:859–875. doi:10.1146/annurev.arplant.57.032905.105329.

Elliott, A., and S.L. Shaw. 2018. Update: Plant Cortical Microtubule Arrays. *Plant Physiol.* 176:94–105.

Errera, L. 1888. Über Zellformen und Siefenblasen. Bot. Cent.bl. 34:395–399.

Facette, M.R., C.G. Rasmussen, and J.M. Van Norman. 2019. A plane choice: coordinating timing and orientation of cell division during plant development. *Curr. Opin. Plant Biol.* 47:47–55.

Fache, V., J. Gaillard, D. Van Damme, D. Geelen, E. Neumann, V. Stoppin-Mellet, and M. Vantard. 2010. Arabidopsis kinetochore fiber-associated MAP65-4 cross-links microtubules and promotes microtubule bundle elongation. *Plant Cell*. 22:3804–3815.

Fauquant, C., V. Redeker, I. Landrieu, J.-M. Wieruszeski, D. Verdegem, O. Laprévote, G. Lippens, B. Gigant, and M. Knossow. 2011. Systematic identification of tubulin-interacting fragments of the microtubule-associated protein Tau leads to a highly efficient promoter of microtubule assembly. J. Biol. Chem. 286:33358–33368.

Flanders, D.J., D.J. Rawlins, P.J. Shaw, and C.W. Lloyd. 1989. Computer-aided 3-D reconstruction of interphase epidermal cells of Datura stramonium reveals assembly. *Development*. 106:531–541.

Gaillard, J., E. Neumann, D. Van Damme, V. Stoppin-Mellet, C. Ebel, E. Barbier, D. Geelen, and M. Vantard. 2008. Two Microtubule-associated Proteins of Arabidopsis MAP65s Promote Antiparallel Microtubule Bundling. *Mol. Biol. Cell*. 19:4534–4544.

Grishchuk, E.L., M.I. Molodtsov, F.I. Ataullakhanov, and J.R. McIntosh. 2005. Force production by disassembling microtubules. *Nature*. 438:384–388.

Gunning, B., and M. Sammut. 1990. Rearrangements of Microtubules Involved in Establishing Cell Division Planes Start Immediately after DNA Synthesis and Are Completed just before Mitosis. *Plant Cell*. 2:1273–1282.

Gupta, M.L., Jr, P. Carvalho, D.M. Roof, and D. Pellman. 2006. Plus end-specific depolymerase activity of Kip3, a kinesin-8 protein, explains its role in positioning the yeast mitotic spindle. *Nat. Cell Biol.* 8:913–923.

Herrmann, A., P. Livanos, E. Lipka, A. Gadeyne, M. Hauser, D. Van Damme, and S. Müller. 2018. Dual localized kinesin-12 POK2 plays multiple roles during cell division and interacts with MAP65-3. *EMBO Rep.* e46085.

Ho, C.-M.K., T. Hotta, F. Guo, R.W. Roberson, Y.-R.J. Lee, and B. Liu. 2011. Interaction of Antiparallel Microtubules in the Phragmoplast Is Mediated by the Microtubule-Associated Protein MAP65-3 inArabidopsis. *Plant Cell*. 23:2909–2923.

Ho, C.-M.K., Y.-R.J. Lee, L.D. Kiyama, S.P. Dinesh-Kumar, and B. Liu. 2012. Arabidopsis Microtubule-Associated Protein MAP65-3 Cross-Links Antiparallel Microtubules toward Their Plus Ends in the Phragmoplast via Its Distinct C-Terminal Microtubule Binding Domain. *Plant Cell*. 24:2071–2085.

Janson, M.E., R. Loughlin, I. Loïodice, C. Fu, D. Brunner, F.J. Nédélec, and P.T. Tran. 2007. Crosslinkers and motors organize dynamic microtubules to form stable bipolar arrays in fission yeast. *Cell*. 128:357–368.

Jürgens, G. 2005a. CYTOKINESIS IN HIGHER PLANTS. *Annual Review of Plant Biology*. 56:281–299. doi:10.1146/annurev.arplant.55.031903.141636.

Jürgens, G. 2005b. Plant cytokinesis: fission by fusion. *Trends Cell Biol.* 15:277–283.

Kellogg, E.H., N.M.A. Hejab, S. Poepsel, K.H. Downing, F. DiMaio, and E. Nogales. 2018. Near-atomic model of microtubule-tau interactions. *Science*. 360:1242–1246.

Kiyomitsu, T. 2019. The cortical force-generating machinery: how cortical spindle-pulling forces are generated. *Current Opinion in Cell Biology*. 60:1–8. doi:10.1016/j.ceb.2019.03.001.

Komis, G., I. Luptovčiak, M. Ovečka, D. Samakovli, O. Šamajová, and J. Šamaj. 2017. Katanin Effects on Dynamics of Cortical Microtubules and Mitotic Arrays in Arabidopsis thaliana Revealed by Advanced Live-Cell Imaging. *Front. Plant Sci.* 8:866.

Laan, L., N. Pavin, J. Husson, G. Romet-Lemonne, M. van Duijn, M.P. López, R.D. Vale, F. Jülicher, S.L. Reck-Peterson, and M. Dogterom. 2012a. Cortical dynein controls microtubule dynamics to generate pulling forces that position microtubule asters. *Cell*. 148:502–514.

Laan, L., S. Roth, and M. Dogterom. 2012b. End-on microtubule-dynein interactions and pulling-based positioning of microtubule organizing centers. *Cell Cycle*. 11:3750–3757.

Lee, Y.-R.J., and B. Liu. 2013. The rise and fall of the phragmoplast microtubule array. *Curr. Opin. Plant Biol.* 16:757–763.

Li, H., B. Sun, M. Sasabe, X. Deng, Y. Machida, H. Lin, Y.-R.J. Lee, and B. Liu. 2017. Arabidopsis MAP65-4 plays a role in phragmoplast microtubule organization and marks the cortical cell division site. *New Phytol.* 215:187–201.

Lindeboom, J.J., M. Nakamura, A. Hibbel, K. Shundyak, R. Gutierrez, T. Ketelaar, A.M.C. Emons, B.M. Mulder, V. Kirik, and D.W. Ehrhardt. 2013. A mechanism for reorientation of cortical microtubule arrays driven by microtubule severing. *Science*. 342:1245533.

Lipka, E., A. Gadeyne, D. Stöckle, S. Zimmermann, G. De Jaeger, D.W. Ehrhardt, V. Kirik, D. Van Damme, and S. Müller. 2014. The Phragmoplast-Orienting Kinesin-12 Class Proteins Translate the Positional Information of the Preprophase Band to Establish the Cortical Division Zone in Arabidopsis thaliana. *Plant Cell*. 26:2617–2632.

Livanos, P., and S. Müller. 2019. Division Plane Establishment and Cytokinesis. *Annu. Rev. Plant Biol.* doi:10.1146/annurev-arplant-050718-100444.

Martinez, P., L.A. Allsman, K.A. Brakke, C. Hoyt, J. Hayes, H. Liang, W. Neher, Y. Rui, A.M. Roberts, A. Moradifam, B. Goldstein, C.T. Anderson, and C. Rasmussen. 2018. Predicting division planes of three-dimensional cells by soap-film minimization. *Plant Cell*. doi:10.1105/tpc.18.00401.

Martinez, P., A. Luo, A. Sylvester, and C.G. Rasmussen. 2017. Proper division plane orientation and mitotic progression together allow normal growth of maize. *Proc. Natl. Acad. Sci. U. S. A.* 114:2759–2764.

Masoud, K., E. Herzog, M.-E. Chabouté, and A.-C. Schmit. 2013. Microtubule nucleation and establishment of the mitotic spindle in vascular plant cells. *Plant J.* 75:245–257.

Mirabet, V., P. Krupinski, O. Hamant, E.M. Meyerowitz, H. Jönsson, and A. Boudaoud. 2018. The self-

organization of plant microtubules inside the cell volume yields their cortical localization, stable alignment, and sensitivity to external cues. *PLoS Comput. Biol.* 14:e1006011.

Mir, R., V.H. Morris, H. Buschmann, and C.G. Rasmussen. 2018. Division Plane Orientation Defects Revealed by a Synthetic Double Mutant Phenotype. *Plant Physiol.* 176:418–431.

Mullen, T.J., and S.M. Wignall. 2017. Interplay between microtubule bundling and sorting factors ensures acentriolar spindle stability during C. elegans oocyte meiosis. *PLoS Genet.* 13:e1006986.

Müller, S., S. Han, and L.G. Smith. 2006a. Two kinesins are involved in the spatial control of cytokinesis in Arabidopsis thaliana. *Curr. Biol.* 16:888–894.

Müller, S., S. Han, and L.G. Smith. 2006b. Two kinesins are involved in the spatial control of cytokinesis in Arabidopsis thaliana. *Curr. Biol.* 16:888–894.

Murata, T., T. Sano, M. Sasabe, S. Nonaka, T. Higashiyama, S. Hasezawa, Y. Machida, and M. Hasebe. 2013. Mechanism of microtubule array expansion in the cytokinetic phragmoplast. *Nat. Commun.* 4:1967.

Panteris, E., B.-E. Diannelidis, and I.-D.S. Adamakis. 2018. Cortical microtubule orientation in Arabidopsis thaliana root meristematic zone depends on cell division and requires severing by katanin. *Journal of Biological Research-Thessaloniki*. 25. doi:10.1186/s40709-018-0082-6.

Pickett-Heaps, J.D., and D.H. Northcote. 1966. Organization of microtubules and endoplasmic reticulum during mitosis and cytokinesis in wheat meristems. *J. Cell Sci.* 1:109–120.

Pietra, S., A. Gustavsson, C. Kiefer, L. Kalmbach, P. Hörstedt, Y. Ikeda, A.N. Stepanova, J.M. Alonso, and M. Grebe. 2013. Arabidopsis SABRE and CLASP interact to stabilize cell division plane orientation and planar polarity. *Nat. Commun.* 4:2779.

Portran, D., M. Zoccoler, J. Gaillard, V. Stoppin-Mellet, E. Neumann, I. Arnal, J.L. Martiel, and M. Vantard. 2013. MAP65/Ase1 promote microtubule flexibility. *Mol. Biol. Cell*. 24:1964–1973.

Rasmussen, C.G., and M. Bellinger. 2018. An overview of plant division-plane orientation. *New Phytol.* 219:505–512.

Rasmussen, C.G., B. Sun, and L.G. Smith. 2011. Tangled localization at the cortical division site of plant cells occurs by several mechanisms. *J. Cell Sci.* 124:270–279.

Schaefer, E., K. Belcram, M. Uyttewaal, Y. Duroc, M. Goussot, D. Legland, E. Laruelle, M.-L. de Tauzia-Moreau, M. Pastuglia, and D. Bouchez. 2017. The preprophase band of microtubules controls the robustness of division orientation in plants. *Science*. 356:186–189.

Schindelin, J., I. Arganda-Carreras, E. Frise, V. Kaynig, M. Longair, T. Pietzsch, S. Preibisch, C. Rueden, S. Saalfeld, B. Schmid, J.-Y. Tinevez, D.J. White, V. Hartenstein, K. Eliceiri, P. Tomancak, and A. Cardona. 2012. Fiji: an open-source platform for biological-image analysis. *Nat. Methods*. 9:676–682.

Shaw, S.L., R. Kamyar, and D.W. Ehrhardt. 2003. Sustained microtubule treadmilling in Arabidopsis cortical arrays. *Science*. 300:1715–1718.

Smertenko, A. 2018. Phragmoplast expansion: the four-stroke engine that powers plant cytokinesis. *Curr. Opin. Plant Biol.* 46:130–137.

Smertenko, A., F. Assaad, F. Baluška, M. Bezanilla, H. Buschmann, G. Drakakaki, M.-T. Hauser, M. Janson, Y. Mineyuki, I. Moore, S. Müller, T. Murata, M.S. Otegui, E. Panteris, C. Rasmussen, A.-C. Schmit, J. Šamaj, L. Samuels, L.A. Staehelin, D. Van Damme, G. Wasteneys, and V. Žárský. 2017. Plant Cytokinesis: Terminology for Structures and Processes. *Trends Cell Biol.* 27:885–894.

Smertenko, A.P., H.-Y. Chang, V. Wagner, D. Kaloriti, S. Fenyk, S. Sonobe, C. Lloyd, M.-T. Hauser, and P.J. Hussey. 2004. The Arabidopsis microtubule-associated protein AtMAP65-1: molecular analysis of its microtubule bundling activity. *Plant Cell*. 16:2035–2047.

Smith, L.G., S.M. Gerttula, S. Han, and J. Levy. 2001. Tangled1: a microtubule binding protein required for the spatial control of cytokinesis in maize. *J. Cell Biol.* 152:231–236.

Smith, L.G., S. Hake, and A.W. Sylvester. 1996. The tangled-1 mutation alters cell division orientations throughout maize leaf development without altering leaf shape. *Development*. 122:481–489.

Spinner, L., A. Gadeyne, K. Belcram, M. Goussot, M. Moison, Y. Duroc, D. Eeckhout, N. De Winne, E. Schaefer, E. Van De Slijke, G. Persiau, E. Witters, K. Gevaert, G. De Jaeger, D. Bouchez, D. Van Damme, and M. Pastuglia. 2013. A protein phosphatase 2A complex spatially controls plant cell division. *Nat. Commun.* 4:1863.

Spinner, L., M. Pastuglia, K. Belcram, M. Pegoraro, M. Goussot, D. Bouchez, and D.G. Schaefer. 2010. The function of TONNEAU1 in moss reveals ancient mechanisms of division plane specification and cell elongation in land plants. *Development*. 137:2733–2742. doi:10.1242/dev.043810.

Stoppin-Mellet, V., V. Fache, D. Portran, J.-L. Martiel, and M. Vantard. 2013. MAP65 coordinate microtubule growth during bundle formation. *PLoS One*. 8:e56808.

Subramanian, R., E.M. Wilson-Kubalek, C.P. Arthur, M.J. Bick, E.A. Campbell, S.A. Darst, R.A. Milligan, and T.M. Kapoor. 2010. Insights into antiparallel microtubule crosslinking by PRC1, a conserved nonmotor microtubule binding protein. *Cell*. 142:433–443.

Traas, J., C. Bellini, P. Nacry, J. Kronenberger, D. Bouchez, and M. Caboche. 1995. Normal differentiation patterns in plants lacking microtubular preprophase bands. *Nature*. 375:676–677. doi:10.1038/375676a0.

Tulin, A., S. McClerklin, Y. Huang, and R. Dixit. 2012. Single-molecule analysis of the microtubule cross-linking protein MAP65-1 reveals a molecular mechanism for contact-angle-dependent microtubule bundling. *Biophys. J.* 102:802–809.

Van Damme, D., M. Vanstraelen, and D. Geelen. 2007. Cortical division zone establishment in plant cells. *Trends Plant Sci.* 12:458–464.

Walker, K.L., S. Müller, D. Moss, D.W. Ehrhardt, and L.G. Smith. 2007. Arabidopsis TANGLED identifies the division plane throughout mitosis and cytokinesis. *Curr. Biol.* 17:1827–1836.

Wasteneys, G.O., and J.C. Ambrose. 2009. Spatial organization of plant cortical microtubules: close encounters of the 2D kind. *Trends Cell Biol.* 19:62–71.

Winters, L., I. Ban, M. Prelogović, I. Kalinina, N. Pavin, and I.M. Tolić. 2019. Pivoting of microtubules driven by minus-end-directed motors leads to spindle assembly. *BMC Biology*. 17. doi:10.1186/s12915-019-0656-2.

Wong, J.H., and T. Hashimoto. 2017. Novel Arabidopsis microtubule-associated proteins track growing

903 microtubule plus ends. *BMC Plant Biol.* 17:33.

904 Worden, N., E. Park, and G. Drakakaki. 2012. Trans-Golgi Network-An Intersection of Trafficking Cell
905 Wall Components. *Journal of Integrative Plant Biology*. no–no. doi:10.1111/j.1744-
906 7909.2012.01179.x.

907 Wright, A.J., K. Gallagher, and L.G. Smith. 2009. discordia1 and alternative discordia1 function
908 redundantly at the cortical division site to promote preprophase band formation and orient division
909 planes in maize. *Plant Cell*. 21:234–247.

910 Xu, X.M., Q. Zhao, T. Rodrigo-Peiris, J. Brkljacic, C.S. He, S. Müller, and I. Meier. 2008. RanGAP1 is a
911 continuous marker of the Arabidopsis cell division plane. *Proc. Natl. Acad. Sci. U. S. A.* 105:18637–
912 18642.

913 Zhang, Q., E. Fishel, T. Bertroche, and R. Dixit. 2013. Microtubule severing at crossover sites by katanin
914 generates ordered cortical microtubule arrays in Arabidopsis. *Curr. Biol.* 23:2191–2195.

915